Molecular dynamics simulations of ion transport through carbon nanotubes. I. Influence of geometry, ion specificity, and many-body interactions

Titus A. Beu[a)]
Faculty of Physics, University "Babeş-Bolyai", 400084 Cluj-Napoca, Romania

(Received 19 January 2010; accepted 23 March 2010; published online 28 April 2010)

Extensive molecular dynamics simulations of the flow of aqueous NaCl and NaI solutions through carbon nanotubes are presented, evidencing the dependence of diverse transport features on the solute specificity, the nanotube geometry, and the various atomic models employed, including polarizability. The simulated properties are in agreement with published results, indicating that ion translocation sets in only for nanotubes with chiralities higher than (7,7), and extend the explanation of the mechanisms governing ion transport to larger chiralities. The interpretation of the various dynamic quantities is developed in close connection with the structural details of the solution and the energy barriers the solute components have to overcome. Also, the role and relevance of water and ion polarizabilities are discussed in detail. © *2010 American Institute of Physics*.
[doi:10.1063/1.3387972]

I. INTRODUCTION

Since their discovery in 1991,[1] carbon nanotubes (CNTs) have attracted considerable interest due to their exceptional mechanical, chemical, optical, and electronic properties that make them suitable for a wide variety of applications including catalysis, electronics, and molecular sensing.[2]

The recent development of methods for cutting CNTs into small open-ended pipes[3] enabled the arrangement of tubes of controllable sizes[4–7] within membranes[8–10] and filling them with various compounds.[11] Single-walled CNTs have thus become promising materials for nanofluidic and membrane technology, opening perspectives to applications involving filtration. Flow rates have been found to be unexpectedly high and mostly independent of the length of the pores, in contrast with predictions from macroscopic hydrodynamics. Water and ion permeation of nanopores is, on the other hand, a key issue for biological membrane-spanning ion channels and aquaporins, as well as for materials like zeolites and gels.

In order to design nanofluidic devices using nanotubes, a much more detailed understanding of the flow of aqueous solutions through synthetic nanopores is required and the past decade represented a period of concerted experimental and theoretical research efforts to elucidate several of the hitherto incompletely understood aspects. Hummer *et al.*[12] reported molecular dynamics (MD) studies of water conduction through the hydrophobic channel of a CNT. The simulations showed spontaneous and continuous filling of the nonpolar CNT resulting in a pulselike transmission of one-dimensionally ordered water molecules and significant water occupancy despite the reduction in the number of hydrogen bonds compared with the bulk fluid.

The investigation of accurate boundary conditions for the fluid flow in nanopores has been undertaken by Sokhan *et al.*[13] Nicholson and Quirke[14] observed in equilibrium MD simulations of sodium chloride solutions confined in model CNTs that ion pairing can occur along the pore axis, preferentially in narrow nanotubes (of radius up to 0.65 nm). There is a well-ordered layer of water at the wall with gradually vanishing structure as the pore radius increases.

Supple and Quirke[15,16] carried out MD simulations of nanotubes imbibing oil at an oil/vapor interface and evidenced a very rapid imbibition dynamics which does not obey the macroscopic equation for capillary filling. The linear time dependence at short times and the significant increase in the filling speeds, especially for narrow nanotubes [chirality (7,7), $R \simeq 4.8$ Å], are the main predictions of these simulations.

The MD studies of Dzubiella *et al.*[17,18] on the permeation of hydrophobic, structureless, cylindrical nanopores by water and ions have evidenced the intermittent filling of the pore by water under equilibrium conditions for radii larger than a critical value ($R_c \simeq 5.3$ Å). Water can still permeate narrower nanopores, nevertheless under the action of a strong electric field generated by an initial Na^+ ion concentration imbalance between the reservoirs. The cation passages through the pore reduce the electric field until the pore empties of water and closes to further ion transport, providing a possible mechanism for biological ion channel gating.

Peter and Hummer[19] studied computationally the Na^+ ion transport through narrow hydrophobic pores in model membranes formed of hexagonally packed armchair type (10,10) CNT. Two types of membranes have been simulated, one consisting of four parallel open tubes ("sieve" geometry) and the other combining three capped and one open tube ("channel" geometry), both arrangements within a periodi-

[a)]Electronic mail: titus.beu@phys.ubbcluj.ro.

cally replicated unit cell. The subnanometer wide pores appear to pose a huge free-energy barrier for ions, but a small increase in the pore diameter nearly eliminates the barrier. There is a preference of hydrated ions to move along the pore wall rather than through the center of the pore.

Hanasaki and Nakatani[20] investigated the density and temperature dependences of microscopic structure and hydrogen bond dynamics of water inside rigid CNTs using constant energy MD simulations and a smoothly truncated extended simple point charge water model. As the overall density increases, the density profiles of water inside CNTs become sharper and shift closer to the wall.

The MD simulations of Liu *et al.*[21] concerning the permeation of ions and water in a membrane consisting of single wall neutral CNTs revealed changes in the first hydration shell of the ions upon confinement in tubes of up to 0.90 nm effective internal diameter. The authors have also investigated the effects of tube flexibility and found that the radial distribution profiles of Na^+ ions broaden significantly with increasing number of ion pairs in the tube, in contrast to the profiles of the Cl^- ions.

As promising candidates for water desalination using reverse osmosis, membranes incorporating CNTs have been simulated under hydrostatic pressure and equilibrium conditions by Corry.[22] With a view to determine the size and uniformity of tubes required to achieve a desired salt rejection, CNTs ranging in diameter from 6 to 11 Å have been considered. The potential of mean force for ion and water translocation showed that ions face a large energy barrier and will not pass through narrow pores [(5,5) and (6,6) "armchair-type" tubes], but can pass through wider ones [(7,7) and (8,8) nanotubes]. Due to the formation of stable hydrogen bonds, however, water faces no such impediment. The considered membranes thus allow under a hydrostatic pressure difference for high degrees of desalination to be achieved at flow rates exceeding by 4–5 orders of magnitude any existing membranes and the predictions extrapolated from conventional theory.

Recently, Whitby *et al.*[23] reported experimental results for flow of water, ethanol, and decane through nanopipes composed of amorphous carbon with large inner diameters (~43 nm) and found enhanced transport up to 45 times the theoretical predictions.

By using MD simulations, Hilder *et al.*[24] recently inferred that boron nitride nanotubes have superior water flow properties compared with CNTs, and thus can provide a more efficient water purification. Concretely, a (5,5) boron nitride nanotube is reported to yield 100% salt rejection at concentrations as high as 1*M* owing to a high energy barrier while still allowing water molecules to flow at a rate of almost 1 $l/m^2/h$. Furthermore, ions continue to be rejected under the influence of high hydrostatic pressures up to several hundreds of megapascals.

The present work is meant to be a contribution to the elucidation of several aspects regarding the ion and water transport through carbon nanochannels by means of detailed MD simulations. In addition to many aspects addressed in previous publications (relevance of geometrical details, free energy barriers, hydration number of ions etc.), several other aspects are being tackled as well, among which the detailed electrostatics, ion specificity, and relevance of polarizability.

Technically, the present approach shares various methodological details and atomistic models with other reported studies (for example, Refs. 19, 22, 25, and 26) and, partially, has been described elsewhere.[27] There are, however, several modeling differences: (1) the simulations are devoted to *single* CNTs embedded in explicit membranes with graphene walls (replicated virtually by periodic boundary conditions), rather than to membranes that resulted from the close packing of CNTs; (2) the treated CNTs are several times longer in order to reduce the fluctuations of the radial distributions inside the nanotube; (3) rigid-body dynamics and up-to-date site-site interaction potentials are employed for the water molecules; (4) large ensembles of independent initial configurations and significantly longer data collection times for individual trajectories (up to 0.4 μs) are considered, providing substantially better statistics; and (5) the effect of many-body interactions stemming from polarizable molecular and ionic interaction models and accounted for by induced dipole moments is given special emphasis.

The present results are consistent with those from the literature (for example, with those of Peter and Hummer[19] and Corry[22]), confirming that ions face quite significant energy barriers and pass through armchair-type nanotubes only for chiralities higher than (7,7). Moreover, since all nanotubes up to chirality (12,12) are being considered, the results are able to explain also the dominant mechanisms for the ionic conduction and to provide a quantitative image in terms of cation and anion passage rates.

II. SIMULATION DETAILS

A. MD methodology

The reported simulations have been performed entirely by a homemade MD computer code (MDSQUAD) designed to optimally meet the tight accuracy and speed requirements associated with massive nanofluidic calculations.

Among the distinctive modeling aspects of the present approach, a central role is played by the usage of rigid-body dynamics for the water molecules in conjunction with up-to-date polarizable/nonpolarizable site-site potential models, which assure increased accuracy in the description of the transport processes on the microsecond scale of interest. Rigid-body dynamics allows for larger time steps to be used, not in the least by avoiding the necessity (and possible artifacts) of supplementary "shake-type" algorithms,[28] typically required by approaches based on single atom dynamics to preserve the equilibrium structure of molecules. On the other hand, the computations become more efficient by the intrinsic reduction in the number of degrees of freedom to three for translation and three for rotation. Technically, since the common Euler angle representation of the rotational equations of motion is singular for particular angle combinations, the quaternion representation has been employed instead.[28,29] Each triplet of Euler angles is equivalent to four quaternions (subject to a normalization condition) and, thus, seven coordinates have to be propagated for each molecule (instead of

nine, in the particular case of water). A similar formulation based on quaternions was also used by Liu *et al.*[21]

The MD integrator employed both for the translational and rotational degrees of freedom has been a fourth order Gear-type predictor-corrector algorithm,[28] operated typically with a 1 fs time step for the equilibration runs (where substantial gradients and inhomogeneities can occur) and 2.5 fs time step for the production runs. The time step for the production runs has been slightly above the 2 fs employed in most of the recent simulations concerning water and ion transport through CNTs.[17–20,22] However, in order to ascertain the accuracy and to provide an error estimate for the production runs, for selected cases complete reference simulations with a 1 fs time step have been also carried out. It is worthwhile noting that in contrast to approaches relying on single atom dynamics and supplementary molecular reconstruction algorithms, the present rigid-body dynamics implementation actually remains stable in the presence of moderate density, pressure, temperature, and electrostatic field gradients even for larger time steps than the ones reported here.

In order to eliminate surface effects and to ensure a continuous flow of ions and water molecules, periodic boundary conditions in all three directions have been applied. Additionally, to account accurately for the long-range electrostatic interactions of the charges and their periodic images, Ewald sum techniques have been employed. By using the P^3M particle-particle/particle-mesh Ewald method developed by Hockney and Eastwood,[30] as formulated by Deserno and Holm,[31] massive simulations over sufficiently long time intervals (up to several hundreds of nanoseconds) have been possible, allowing for reliable current flows to be measured. Details on the electrostatics are provided in Appendix A.

A Gaussian thermostat[28] was implemented for the translational degrees of freedom of the water molecules, preventing the system from heating (due to structural relaxation or particle transport in the presence of applied electric fields) and fixing its temperature at 300 K. While continuously rescaling the particle velocities, the Gaussian thermostat does not alter the velocity distribution itself. The degrees of freedom for the rotation of the water molecules and the translation of the ions have been allowed to relax freely to the equilibrium temperature.

B. Force field

One of the two molecular representations implemented for water has been the rigid nonpolarizable four-site model TIP4P of Jorgensen *et al.*,[32,33] intensively used now for more than two decades in simulations of aqueous solutions and clusters and known to describe more accurately than older three-site models the thermodynamic and structural properties of water.

The second molecular representation adopted for water has been a polarizable one, namely, the five-site model developed by Yu and van Gunsteren,[34] denoted as COS/G2 and belonging to the category of the so-called charge-on-spring (COS) models.[35] Specifically, polarization is accounted for via an induced dipole moment represented by a pair of charges of fixed value (typically, several charge units), which can be relocated self-consistently with a relative separation (typically, several percent of an angstrom) determined by the local electric field. Evidently, COS models take only the first-order linear polarization effect into account.

TABLE I. Parameters for the implemented water models.

	TIP4P	COS/G2
r_{OH} (Å)	0.9572	0.9572
r_{OS} (Å)	0.15	0.22
θ_{HOH} (deg)	104.52	104.52
ϵ_O (kJ/mol)	0.648 954	0.761 04
σ_O (Å)	3.153 65	3.196 02
q_H (e)	0.52	0.5265
q_{pol} (e)	0	−8
α_{pol} (Å^3)	0	1.255
References	32, 33	34

In particular, the polarizable COS/G2 model features three fixed atomic sites (on the O and H atoms) and a pair of virtual polarization sites: a *fixed* site S located on the bisector of the fixed HOH angle in the proximity of the O atom and a *movable* site M, which can be repositioned with respect to the former. Electric charges are carried by the H atoms ($2q_H$), the fixed polarization site ($-2q_H-q_{pol}$), and the movable polarization site (q_{pol}). The oxygen atom exhibits only Lennard-Jones interactions with all other van der Waals sites present in the system.

The induced dipole μ^{ind} of a particular water molecule is determined by the total electric field $\mathbf{E}_S$ acting on the fixed polarization site and, technically, it implies the self-consistent relocation of the movable site at a relative position $\mathbf{r}_{SM}$ from the fixed one given by

$$\mu^{ind} = \alpha_{pol}\mathbf{E}_S = q_{pol}\mathbf{r}_{SM}, \tag{1}$$

where α_{pol} is the molecular polarizability. Clearly, in the absence of an electric field, the positions of the two polarization sites coincide.

The relevant geometry and interaction parameters for the employed water models are summarized in Table I. For consistency reasons, we have treated by a COS-type model also the polarizability of the individual ions, associating them a supplementary polarization site whose relative position is determined self-consistently by the electric field experienced by the ion. A beneficial side effect of this treatment in terms of computational efficiency resides in the fact that the overall electrostatics of the system relies solely on point charges, avoiding the necessity of a separate description for dipoles.

As solute anions, besides the Na^+ cation, we have selected two representative halides from the Hofmeister series, i.e., chloride and iodide, which are known to have a different enough behavior to suggest general trends within the series. The actual electrostatic and Lennard-Jones parameters pertaining to the solute ions and the carbon atoms composing the nanotubes are summarized in Table II. The parameters for the van der Waals interactions between different atomic species have been obtained by the Lorentz–Berthelot mixing rules and a cutoff of 10 Å was used throughout.

TABLE II. Parameters for the employed atomic species.

	Na^+	Cl^-	I^-	C
ϵ (kcal/mol)	0.13	0.10	0.10	0.0859
σ (Å)	2.3500	4.3387	5.1500	3.3997
q (e)	+1	−1	−1	0
q_{pol} (e)	−8	−8	−8	0
α_{pol} (Å^3)	0.24	3.25	6.90	0
References	36	37	38	40

The overall methodology and, in particular, the polarizability models used in the present study have been validated by calculations regarding the now well-studied phenomenon of anion-specific surface affinity characterizing the halide solution/air interfaces.[39] Details on the performed simulations and the resulted density profiles, confirming the preferential surface affinity of the iodide ions when polarizability is being accounted for, are presented in Appendix B.

The execution speed of the MDSQUAD code based on the models described above reaches in typical CNT simulations (without polarizability) of 2.4 ns/day/core on up-to-date processors.

C. Channel model

The channel model considered in the present study consists of a rigid nonpolar armchair-type (n,n) CNT of length $2z_{pore}=60.17$ Å ($24\frac{1}{2}$ unit cells), extending symmetrically along the z-axis between two neutral graphene planes located at $\pm z_{pore}$ and two reservoirs formed on either side of the membrane. Along with the different pore radii, r_{pore}, all structural details are specified in Table III. With a view to reducing the statistical errors of the relevant radial distributions, however, not by modeling closely packed *arrays* of parallel CNTs, the *individual* channels investigated here are roughly three times longer than the (10,10) CNTs employed by Peter and Hummer[19] and more than four (respectively two) times than the (8,8) [respectively (6,6)] nanotubes dealt with by Corry.[22] Equally, the water layer solvating the membrane is in the present case significantly thicker.

The *effective* pore radius and pore half length have been defined with respect to the corresponding geometrical values as $r_{pore}^{eff}=r_{pore}-\sigma_{graph}$ and, respectively, $z_{pore}^{eff}=z_{pore}+\sigma_{graph}$, where $\sigma_{graph}=1.674$ Å is half the graphite interplane distance. The latter value is fairly close to the commonly used van der Waals radius for carbon (1.7 Å) and the definitions of the effective dimensions are equivalent to those employed by Corry.[22]

The extent of the simulation cell containing the system, $(-x_{cell},x_{cell})\times(-y_{cell},y_{cell})\times(-z_{cell},z_{cell})$, has been adjusted in all cases such as to produce a reference water density of 1 g/cm^3 relative to the effective total volume. With the above definitions, the latter can be expressed as $V_{fill}^{eff}=8x_{cell}y_{cell}(z_{cell}-z_{pore}^{eff})+2\pi(r_{pore}^{eff})^2z_{pore}^{eff}$. Whereas $2x_{cell}$ and $2y_{cell}$ are constrained to be multiples of graphene elementary cell dimensions, z_{cell} can be fine tuned to yield the desired density.

Consistent with the described geometrical details and the intention of treating solutions based on average on *normal* water density, the NaCl and NaI solutions have been modeled by 1000 water molecules. The 15 solute ions of each species resulted in a concentration of approximately 0.83M relative to the effective model volume and the simulated systems have been thus large enough to achieve fair statistics, but still maintained tractable the numerous and very demanding simulations carried out on the microsecond scale. Peter and Hummer[19] modeled much more diluted solutions, with up to five pairs of Na^+ and Cl^- ions in 516 TIP3P water molecules (~0.2M ionic concentration). The simulations of Corry[22] have been conducted with a similar ionic concentration (0.25M).

In order to drive the ions through the channel, a homogeneous electric field of 0.02 V/Å (in the range of typical physiological conditions in biological ion channels) was applied parallel to the z-axis. This field is about an order of magnitude lower than the one employed by Dzubiella *et al.*[17,18]

Nanotubes of length 30.7 Å have also been investigated and, essentially, similar results to the ones for the nanotubes of length 60.17 Å have been obtained. However, due to the significantly better statistics provided, solely the longer channels will be discussed further on.

D. Trajectory ensembles

In the case of the simulations dealing with nonpolarizable water and ions, for each solute type and particular nanotube radius, a total of 400 ns of data collection was sampled with a time step of 2.5 fs and a storage interval of 2.5 ps. The data collection times used typically in the literature are significantly lower (up to 12 ns with a time step of 2 ns for Peter and Hummer[19] and up to 25 ns for Corry[22]). With a view to reduce time correlations and improve statistics by better sampling the phase space, the measurements have been actually compiled from 32 trajectories of 12.5 ns, each started from a different random initial configuration. Since the computational effort is typically several times higher when including water and ion polarizability (depending on

TABLE III. Geometry of the simulated nanotubes (all dimensions are in angstrom).

Chirality	r_{pore}	r_{pore}^{eff}	z_{pore}	z_{pore}^{eff}	x_{cell}	y_{cell}	z_{cell}	$V_{pore}^{eff}/V_{fill}^{eff}$	C atoms
(8,8)	5.42	3.74	30.09	31.76	14.89	14.74	47.21	0.09	1368
(9,9)	6.09	4.42	30.09	31.76	14.89	14.74	46.58	0.13	1436
(10,10)	6.77	5.10	30.09	31.76	14.89	14.74	45.85	0.17	1522
(11,11)	7.45	5.77	30.09	31.76	14.89	14.74	45.01	0.22	1606
(12,12)	8.12	6.45	30.09	31.76	14.89	13.51	45.19	0.28	1630

the number of iterations needed to converge the induced dipoles), this aspect has been accounted for only in the case of the NaI solution, for which, in view of the results obtained in the benchmark simulations for air/solution interfaces (see Appendix B), the effect of polarizability is expectably more significant. The 200 ns of data collection achieved in this case has been compiled for each particular CNT from 16 independent trajectories of 12.5 ns each.

The preparation of the initial configurations was accomplished starting from an initially empty channel and densely filled reservoirs, allowing the subsequent relaxation of the solution inside the channel, and equilibrating the system for 1 ns. The details of the actual protocol are described in Appendix C. A similar initialization was implemented also by Liu *et al.*,[21] except that in their case the NaCl solution fills initially only one of the reservoirs. With a length of only 23.6 Å, their two CNTs of chiralities (15,0) and (16,0) are of comparable radius with our (8,8) and (9,9) CNTs, respectively. The usage of rigid-body dynamics for water and the quaternion formulation for the rotation is a common point, even though the models for water are different (SPC-Simple Point Charge and, respectively, TIP4P) and we use in addition Ewald sum techniques for the proper representation of the long-range Coulomb interactions. On the other hand, Liu *et al.* use a considerably higher ion concentration (2.26 mol/l).

In order to estimate the errors associated with the ensemble-averaged quantities, we have carried out for the intermediate nanotube (10,10) 400 ns of similar simulations to those described above, however, with a time step of 1 fs instead of 2.5 fs. As will be seen in Sec. III, the absolute difference for most of the quantities of interest is fairly small and provides both an estimate for the time integration error and, given the independent trajectories composing the ensembles, an estimate of the dispersion within the ensembles as well.

III. RESULTS AND DISCUSSION

A. Solution structuring

Snapshots from a typical run for the (10,10) nanotube, showing both the atomic arrangement and the channel structure, are depicted in Fig. 1. Whereas water structuring parallel to the membrane walls is visible in the side view, an even more pronounced radial concentration of water is apparent along the channel in the top view. The appreciable average distance of the solution constituents to the hydrophobic nanotube walls is also characteristic.

Figure 2 offers a qualitative comparison between the ion current composition in the cases of the CNTs of chiralities (8,8), (10,10), and (12,12) by showing the instantaneous z-positions of the ions over typical simulation intervals of 4 ns. The flow through the (8,8) channel involves equally rare passages of anions and Na^+ cations, even though the latter are in terms of the Lennard-Jones parameter σ roughly two times smaller (see Table II). The intermediate nanotube (middle panel) marks the transition from a flow with scarce, only accidental ion passages to a "gating" regime, in which cascades of cations accompanied by rare sinuous anion passages are interrupted by cascades in which the ions reverse the roles and the pore is able to accommodate simultaneously both species of transiting ions. In the (12,12) nanopore (lower panel) the two solute ion species cross the channel on average in opposite directions at comparable rates and several ions of both species may be accommodated by the pore simultaneously. Quite frequently, cations and anions pair and cover jointly portions of the pore.

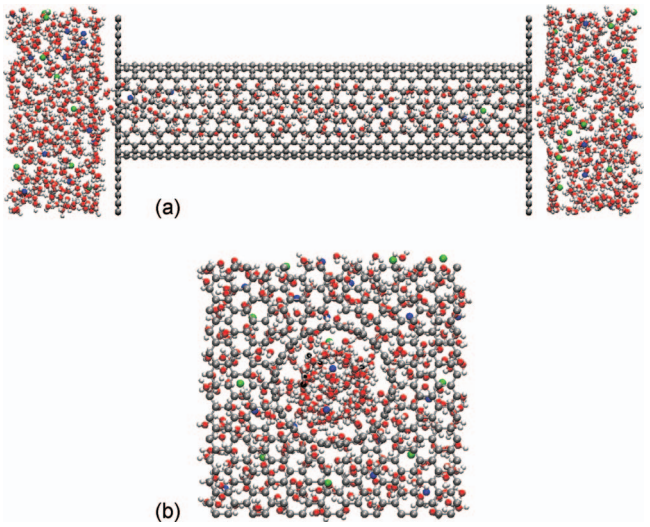

FIG. 1. Snapshot (side and top views) from a typical simulation for the CNT (10,10) (of radius 6.77 Å and length 60.17 Å). The size of the simulation cell is $29.78 \times 29.47 \times 91.70$ Å^3.

The ensemble-averaged radial and axial density profiles plotted in Figs. 3 and 4 provide a detailed picture of the solution structuring in the proximity of the carbon walls. Throughout the paper, the color scheme is used according to which blue stands for Na^+, green for Cl^-, and pink for I^-. Continuous lines and empty symbols indicate the neglect of polarizability, while dashed lines and filled symbols its inclusion. Regardless of the pore radius, water forms well-defined boundary layers both inside the channel and near the mem-

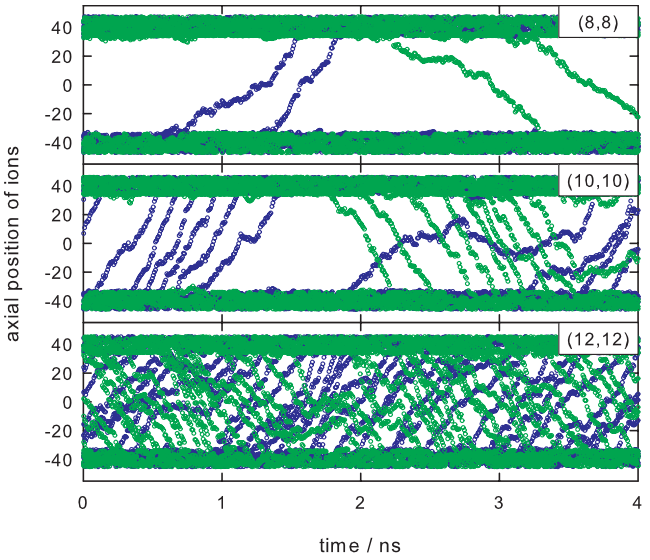

FIG. 2. Axial positions of (nonpolarizable) anions (green) and Na^+ cations (blue) in typical runs for the CNTs (8,8), (10,10), and (12,12).

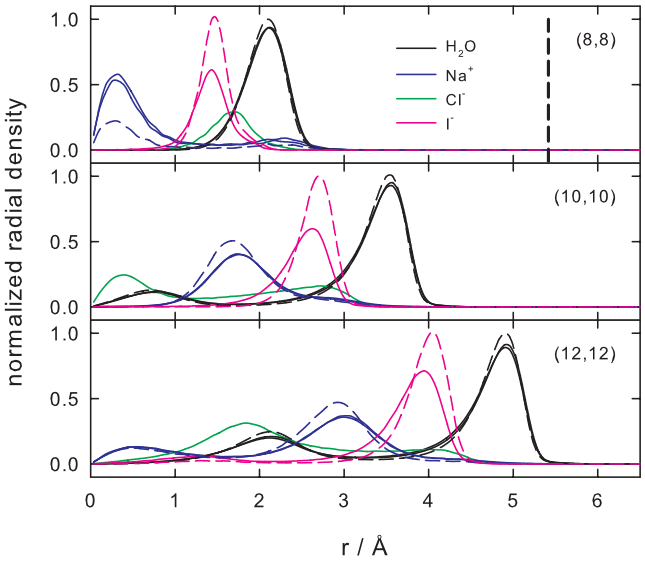

FIG. 3. Normalized average radial density profiles for water and ions for the CNTs (8,8), (10,10), and (12,12). The ion profiles are normalized in each case to the maximum radial density of both ion species. Dashed lines indicate the usage of polarizable water and I^- ion models. The dashed drop line in the upper panel shows the position of the carbon wall for the (8,8) CNT.

brane surfaces (at a distance of roughly 3.2 Å). These significant density maxima are followed toward the solution bulk by a sequence of density maxima, decreasing in the case of the axial profiles toward the constant value within the reservoirs. Since the density profiles result from the direct binning of the positions of the solution components, the radial profiles imply angular integration and thus include the factor $2\pi r$. The longitudinal profiles are evidently nonsymmetric, since the cations and anions driven by the external electric field tend to accumulate on opposed sides of the membrane in their struggle to enter the channel.

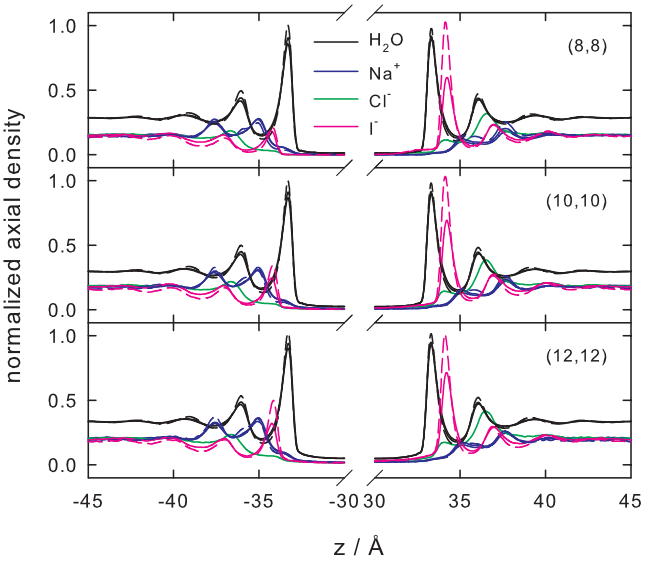

FIG. 4. Normalized average axial density profiles for water and ions for the CNTs (8,8), (10,10), and (12,12). The ion profiles are normalized in each case to the maximum axial density of both ion species. Dashed lines indicate the usage of polarizable water and I^- ion models. The positions of the carbon membrane walls coincide with the z-axis breaks (the pore interior is excluded).

The cylindrical water layers formed inside the channel (Fig. 3) enclose alternating regions of peaking solute ion density, which correspond not necessarily to average static positions, but rather to more probable paths taken by the ions during their passages through the channel. While in the case of the narrowest nanotube the transiting Na^+ ions occupy the central region, forcing both anion species to pass on average in the vicinity of the water boundary layer, with increasing channel radius the tendency of the I^- ions to preserve this arrangement and of the smaller Cl^- ions to pass closer to the axis switching positions with the Na^+ ions, becomes apparent. This behavior is obviously a consequence of the fact that the anions can optimize their hydration shell in the narrow CNTs only near the water boundary layer, while in the wider CNTs [starting with (10,10)], the smaller Cl^- ions can satisfy their hydration number also in the neighborhood of the secondary water density maximum. As such, a well defined ordering of the density maxima is established for larger channel radii and replicated toward the interior depending on the solute type: (H_2O, I^-, Na^+) and, respectively, (H_2O, Na^+, Cl^-).

The radial and axial structuring of water in the case of the (10,10) CNT is generally similar to the one produced in the equilibrium pore filling simulations of Nicholson and Quirke.[14] As for the ions, the very demanding statistics in equilibrium runs makes the corresponding profiles less conclusive and much more difficult to compare. An even more illustrative comparison can be made with the radial density profiles reported by Peter and Hummer for the CNT (10,10) (Fig. 2 of Ref. 19). The positions of the water boundary layer (at about 3.5 Å from the axis) and of the density peak of the Na^+ ions (at about 1.7 Å from the axis) can be seen to agree perfectly despite the different length and the nanotube models. Equally, the Na^+ ion depletion in the region near the tube axis is another common point.

The agreement with the radial water density maxima inside the CNTs (8,8), (10,10), and (12,12) reported by Hanasaki and Nakatani[20] for 300K is also worthwhile mentioning. Quite in contrast, the water and ion peaks in the radial density profiles of Liu *et al.* (Fig. 4 of Ref. 21) for the CNT (16,0) [of comparable radius with our (9,9) pore] appear to be significantly closer to one another and to have a different ordering from the present ones, with no water boundary layer and instead a Na^+ cylindrical shell close to the carbon wall.

The inclusion of polarizable models for water and solute ions (indicated by dashed lines) does not appear to affect in any way the structuring of water and only insignificantly the positions of the ion density peaks (both radially and longitudinally). Instead, polarizability influences to a great extent the relative ion abundance, the I^- anions showing, as a general rule, substantially increased densities in the proximity of the water boundary layers. From this perspective, the channel turns out to accommodate a larger number of I^- anions when polarizability is accounted for, creating a charge imbalance since the Na^+ ions remain practically unaffected for the wider nanotubes. Equally, polarizability significantly increases the accumulation of I^- ions at the right channel entrance.

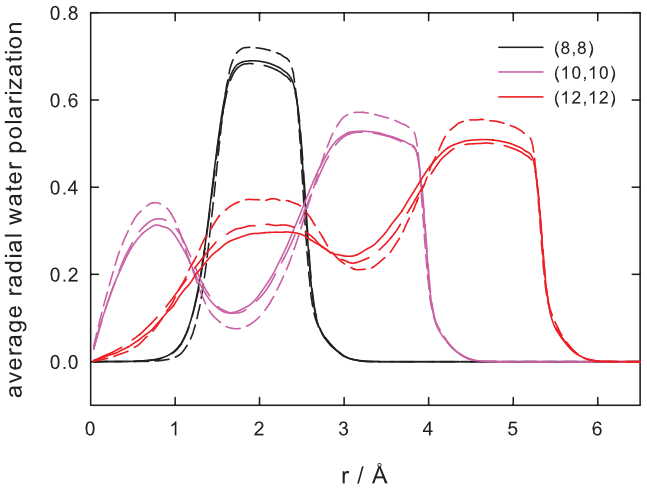

FIG. 5. Longitudinally averaged water polarization inside the CNTs (8,8), (10,10), and (12,12) as a function of the radial coordinate. Continuous lines correspond to NaCl solution, long-dash lines to NaI solution without polarizability, and short-dash lines to polarizable water and ions.

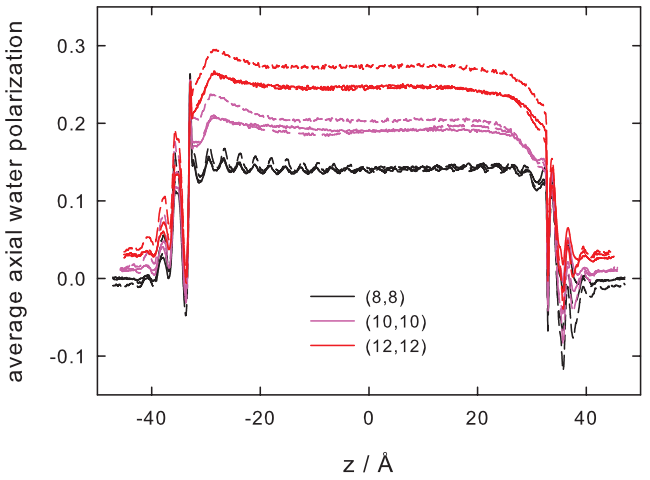

FIG. 6. Transversally averaged water polarization for the CNTs (8,8), (10,10), and (12,12) as a function of the axial position. Continuous lines correspond to NaCl solution, long-dash lines to NaI solution without polarizability, and short-dash lines to polarizable water and ions.

B. Water polarization

It is instructive to examine the water polarization, defined as cosine of the angle made by the electric dipole of the water molecules with the direction of the applied electric field (channel axis), averaged over ensemble, time, and longitudinal/transversal coordinates. Individual ion passages are accompanied by a pronounced water polarization and subsequent relaxation. As compared with the reservoirs, the channel exhibits large polarization fluctuations and a more rapid relaxation due to the smaller number of contained solution components.

The longitudinally averaged radial water polarization profiles shown in Fig. 5 for the *interior* of the nanotubes of chiralities (8,8), (10,10), and (12,12) are centered basically around the positions of the cylindrical water layers (predominantly around the boundary layers), being rather broadly structured. When neglecting polarizability, the little difference between the profiles for the NaCl and NaI solutions is easily noticeable. Nevertheless, polarizable models bring about an increase in the average water polarization of about 10%. In relative terms, the polarization of the boundary layer decreases with increasing pore radius, however, accompanied by the appearance of additional secondary polarization peaks.

Besides being much more significant within the pore than in the reservoirs, the transversely averaged axial water polarization (Fig. 6) features large fluctuations at the membrane, which follow the average axial density maxima of both water and solute ions. With increasing pore radius, the average axial polarization shows an overall increase along the entire nanotube and this comes about through the appearance of the additional radial polarization peaks. Whereas there is little difference between the profiles for NaCl and NaI solutions, the inclusion of polarizability in the case of NaI markedly increases the water polarization in wider nanotubes (by up to 10%). In particular, the axial polarization profiles for NaCl and NaI with/without polarizability are essentially similar in the (8,8) nanotube and show, in addition, a well defined structuring inside the pore, which reflects roughly the atomic structure of the CNT.

C. Potential of mean force and electrostatic potential

The axial potential of mean force (PMF) profiles, calculated as $\mathrm{PMF}(z) = -k_B T \ln(\langle P(r,z)\rangle_r)$ from the transversely averaged position probabilities and shown in Fig. 7, evidence the manifest preference of the anions to reside on average within the reservoirs (being acted upon by forces vanishing in the bulk). The inclusion of polarizable models leads to hardly distinguishable profiles, which have not been represented. In the vicinity of the boundary layers, the profiles show pronounced free energy minima around the positions of the corresponding density maxima. It can be seen that ions face an appreciable energy barrier to enter the tube, which significantly increases with decreasing pore radius. The energy barrier increase is, however, less pronounced for the water molecules.

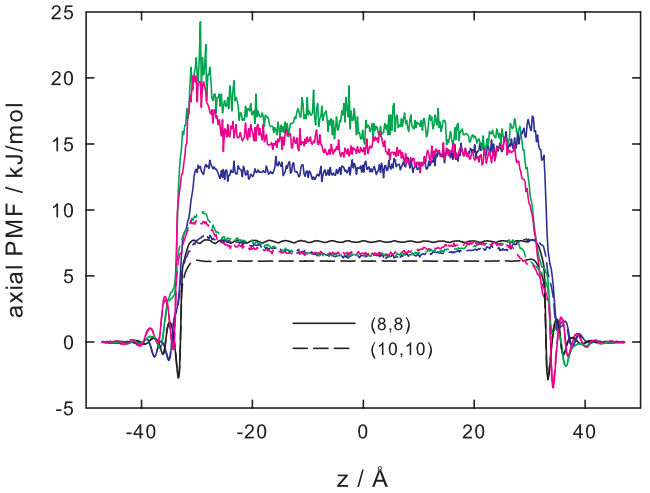

FIG. 7. Axial PMF profiles derived from the average densities of the components of the NaCl and NaI solutions in the CNTs (8,8) and (10,10). Black stands for water, blue for Na^+, green for Cl^-, and pink for I^-.

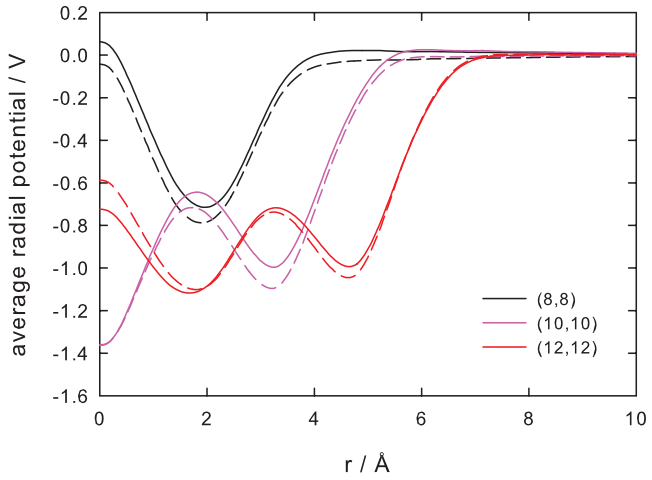

FIG. 8. Average radial electrostatic potential inside the CNTs (8,8), (10,10), and (12,12). Continuous lines correspond to the NaCl solution and short-dash lines to the NaI solution with polarizable water and ions.

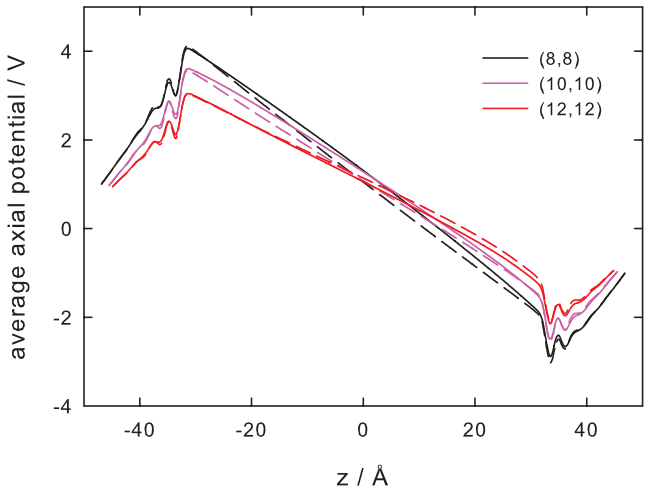

FIG. 9. Average axial electrostatic potential for the CNTs (8,8), (10,10), and (12,12). Continuous lines correspond to the NaCl solution and short-dash lines to the NaI solution with polarizable water and ions.

For the wider CNTs the profiles corresponding to ions are almost flat (discretely bent) and largely overlapping inside the pore, indicating that the ions move almost frictionless through the pore, as noted also by Corry.[22] As direct consequence, the conductance of water through these CNTs is largely independent of their length and our simulations for CNTs of half length prove this point unambiguously. By contrast, for the (8,8) CNT the profiles for the cations and anions have nonvanishing opposite slopes, making the translocation of the ions more difficult. Moreover, in this case, also a difference between the two anion species can be noticed, namely, a lower free energy barrier for the I^- ions, rendering their passages more probable.

In the case of the (10,10) CNT, the PMF compares qualitatively well with the profile reported by Peter and Hummer[19] for their three times shorter channel of same chirality. In the present case, the free energy barrier is on average slightly higher (by approximately 1 kJ/mol) and considerably clearer structured outside the pore due to the less closer packaging of the virtually replicated nanotubes and the more significant influence of the membrane. Confirming the influence of the membrane, for the sieve geometry (made up exclusively of open closely packed CNTs) there is a further decrease of 2 kJ/mol in the results of Peter and Hummer.

The average radial and axial electrostatic potential profiles plotted in Figs. 8 and 9 reflect general features of the field determined jointly by the solution components and the external electrostatic field. Common findings for both types of profiles are their little dependence on the anion species and on the inclusion of molecular and ionic polarizability, but, at the same time, the significant influence of the nanotube radius.

In the case of the radial potential (Fig. 8), the position of the outer minimum follows essentially the water boundary layer for all nanotube sizes. Additional minima appear with increasing pore radius around the secondary water density maxima. With respect to the narrowest pore, for the wider ones there is an obvious (albeit nonmonotonous) increase in the depth of the outer potential minimum. Even though there are practically no differences between the profiles for the nonpolarizable solutes, the inclusion of polarizable models for the NaI solution can be seen to slightly deepen the outer minimum.

The transversely averaged axial potential profiles (Fig. 9) show an abrupt rise, marked by oscillations in the region of the water boundary layers from the reservoirs and an almost linear descent within the nanotube. The potential drop is found mainly across the channel, reflecting the formation of a spatial charge (electrochemical double layer) at the membrane walls, which partially neutralizes the applied electric field in the reservoirs. The net height of the electrostatic potential barrier the charged particles have to overcome to enter the nanotube decreases with increasing pore radius, i.e., the nanotube becomes more permissive to the ion passages, as expected. The profiles for the two nonpolarizable solutes are practically identical and slightly bent within the pore, while the inclusion of polarizable models appears to straighten them.

D. Synthetic structural parameters

In order to characterize synthetically and to compare the flow through the nanotubes, several structural, electrostatic, and dynamic parameters have been examined. The average radial and longitudinal structuring of the solution can be described concisely in terms of the positions of the density peaks of water and ions. The particular reference to the carbon walls is useful to emphasize the generally little dependence of the pattern of density maxima on the pore radius, on the solute type, and on the inclusion of polarizable models, reflecting the basically similar and invariant structuring in the vicinity of the carbon walls. Indeed, the positions of the radial density maxima with respect to the carbon walls depicted in Fig. 10 as functions of the pore radius illustrate this feature. As one can easily notice, the water boundary layer is formed invariably for both solute types, with/without polarizability, both inside the pore and at the membrane walls at a distance of roughly 3.2 Å for all nanotube radii. Equally, the densities of the I^- and Na^+ ions peak unchangingly at about 4.1 and, respectively, 5.0 Å from the carbon walls.

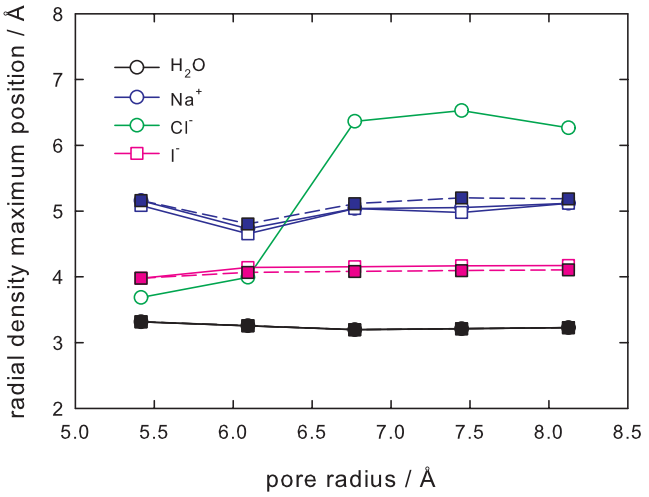

FIG. 10. Positions of the radial density maxima for water and ions with respect to the carbon wall as functions of the nanotube radius. Filled symbols and dashed lines indicate the usage of polarizable models.

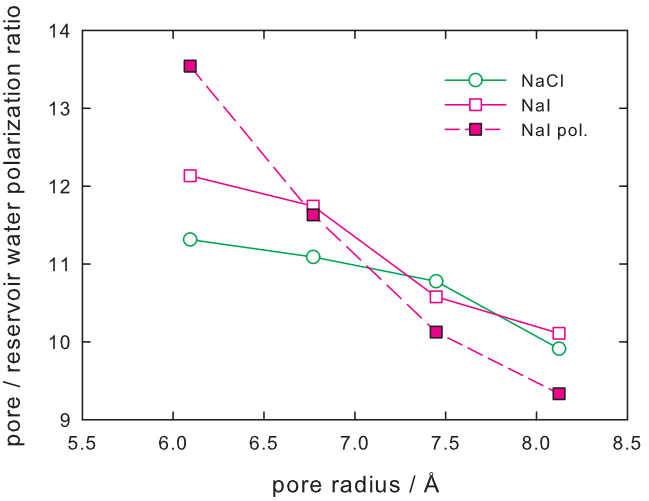

FIG. 12. Pore/reservoir water polarization ratios for the NaCl and NaI solutions as functions of the nanotube radius. Filled symbols and dashed lines indicate the usage of polarizable models.

There is, however, a notable exception from the evoked pattern. It occurs in the radial distribution of the Cl^- anions inside the narrow nanotubes of chiralities (8,8) and (9,9) (Fig. 10), which are seen to accommodate Cl^- preferentially *between* the water boundary layer and the inner Na^+ layer (as also seen from the radial density profiles in Fig. 3). This contrasts with the wider pores, in which the Cl^- maximum density layer is located closer to the axis, *inside* the main Na^+ layer, at about 6.4 Å from the carbon wall, where the chloride ions can optimize their hydration shell.

For all solution components, the pore/reservoir average density ratio (Fig. 11) increases with the pore radius, following approximately the ratio $V_{\text{pore}}^{\text{eff}}/V_{\text{fill}}^{\text{eff}}$ (see Table III). The roughly parabolic profile for water is clearly independent on the solute type and on the inclusion of polarizability. In the case of the ions, due to their relatively small number, but also due to the discrete jumps in the pore radius and the appearance of new density maxima, the profiles are affected by fluctuations. The inclusion of polarizability in the case of the NaI solution appears to induce a slight charge separation, which is consistent with the increase in the radial and axial density maxima for polarizable I^- illustrated in Figs. 3 and 4.

Despite the increasing number of ions inside the channel accompanying the radius increase, as seen from Fig. 12, the ratio of the average water polarizations in the pore and in the reservoirs decreases significantly. This is obviously a consequence of the dissipation of the polarization effect over a larger number of water molecules inside the pore. While neglecting polarizability the profiles corresponding to the two solute types are qualitatively similar, consideration of polarizable models brings about a significant increase in the average water polarization inside the narrowest CNTs.

The pore radius dependence of the transversely averaged electrostatic potential drop across the channel, shown in Fig. 13, is almost linear and clearly insensitive to the solute type or consideration of polarizable models. While the potential difference between the two nanopore ends caused solely by the applied electric field amounts to 1.2 V, the transversely

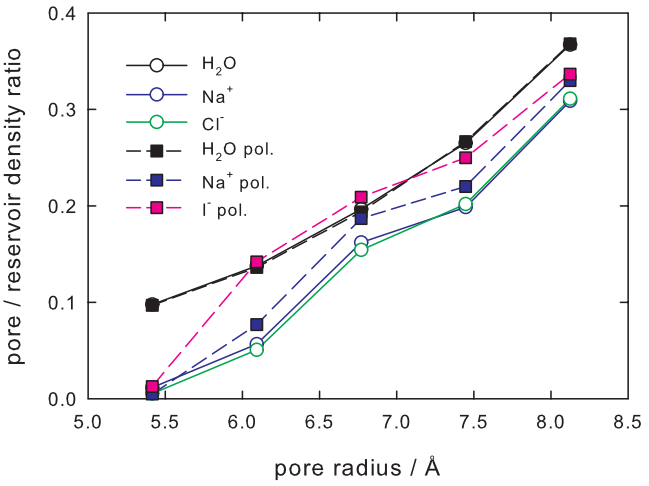

FIG. 11. Pore/reservoir density ratios for water and ions as functions of the nanotube radius. Filled symbols and dashed lines indicate the usage of polarizable models.

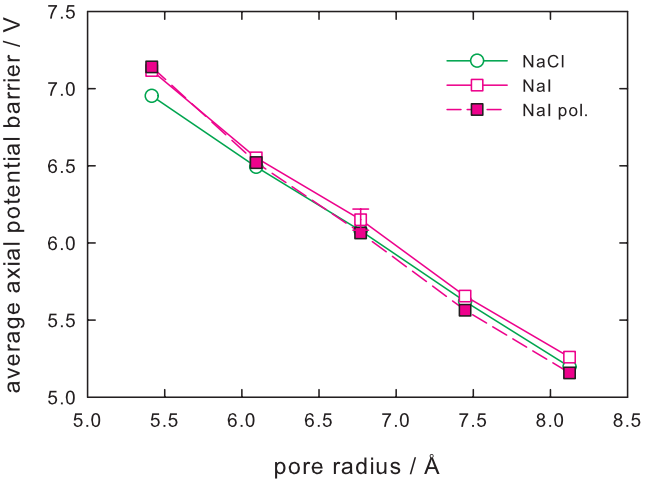

FIG. 13. Average axial electrostatic potential barriers for the NaCl and NaI solutions as functions of the nanotube radius. Filled symbols and dashed lines indicate the usage of polarizable models. The error bars represent the double difference between the values obtained using the time steps of 1 and 2.5 fs.

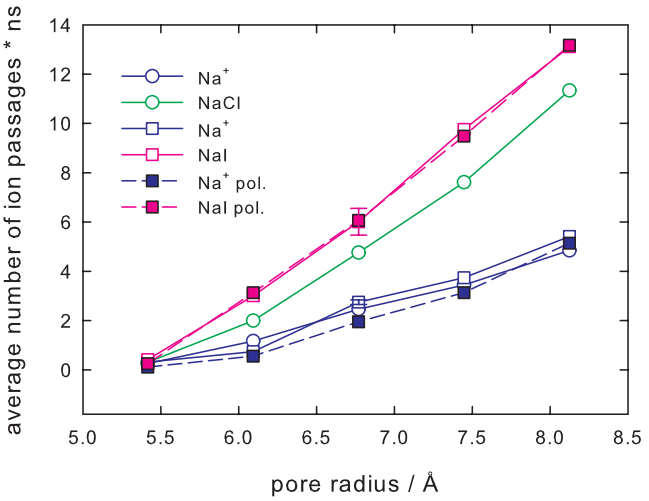

FIG. 14. Average total numbers of ion passages per nanosecond for the NaCl and NaI solutions as functions of the nanotube radius. The partial currents due to the Na^+ ions solely are plotted with blue lines and symbols. Filled symbols and dashed lines indicate the usage of polarizable models. The error bars represent the double difference between the values obtained using the time steps of 1 and 2.5 fs.

averaged potential barriers which have to be overcome by the ions to enter the pore are significantly higher and decrease from about 7 to about 5 V with increasing pore radius. They are clearly a consequence of the formation of electrical double layers at the membrane walls, as discussed before. In order to give an indication on the magnitude of the statistical fluctuations associated with the axial potential barrier, we have plotted for the intermediate nanotube of chirality (10,10) as error bar the double difference between the results obtained from the complete ensembles of trajectories propagated with time steps of 1 and 2.5 fs, respectively. The initial configurations and thus the trajectories being completely different for the two ensembles, the error bar can be considered to cover both the time integration error and the mean standard deviation of the ensemble averages.

E. Transport properties

One of the most significant transport features of the present simulations regards the pore radius dependence of the ionic current, the latter being expressed as the net total number of ions transiting the pore per nanosecond, while considering, obviously, opposite reference directions for anions and cations (Fig. 14). In order to discern the contributions of the different ion species to the total ionic current, the passage rates due to the Na^+ cations solely have been plotted also. In the case of the NaI solution, the profiles corresponding to polarizable models have been depicted as well.

As a first finding, the ion currents show a strong dependence on the pore radius. The (8,8) CNT appears to be very little permeable to ions, enabling under all conditions low currents of about 0.05 nA, which are in line with the results of Dzubiella *et al.*,[17,18] Peter and Hummer,[19] and Corry,[22] evidencing the impermeability for chiralities lower than (7,7). Considering as reference the (8,8) CNT, an increase of 0.68 Å (11%) in the channel radius produces through the (9,9) CNT currents which are over six times more intense, i.e., 0.32 nA for the NaCl solution and 0.48 nA for the NaI solution. A radius increase of 2.7 Å (33%) produces through the (12,12) CNT currents over 30 times more intense, namely, 1.8 nA for the NaCl solution and 2.1 nA for the NaI solution. Qualitatively, the ion current profiles appear to be roughly parabolic and shifted such as to practically vanish for the (8,8) nanopore.

Second, a distinct (albeit limited) selectivity of the CNTs to the anion species is recognizable, the total currents corresponding to the NaI solution exceeding on average by 30% the ones for the NaCl solution. This can be straightforwardly corroborated with the radial profiles of Fig. 3, which illustrate that compared with Cl^-, the I^- anions transit the CNTs preferentially via cylindrical layers of larger average radius, which can hydrate a larger number of ions. Moreover, the lower free energy barrier found for the I^- ions supports the same idea. However, it is interesting to note that irrespective of the solute type and inclusion of polarizable models, the partial Na^+ ion currents coincide within statistical errors and this can be linked with the relative invariability of their spatial profiles under different conditions. On the other hand, the partial Na^+ currents appear to drop to less than 50% of the total currents for the wider CNTs, implying that despite their significantly smaller size, the Na^+ ions transit the pores at lower rates than the larger anions. This can be related again to the particular radial position and relative magnitude of their density maxima inside the pore, but also to their average passage times discussed below. For example, in the case of the NaCl solution the contribution of the Na^+ ions to the total current drops from 59% for the CNT (9,9) to 43% for the CNT (12,12).

Another insight gained from Fig. 14 is that the inclusion of polarizability has little relevance for the ionic currents, in contrast to the case of the spatial density profiles, for which the local relative magnitudes have been found sensitive to polarizability.

As an illustration of the errors associated with the ionic currents, the error bars corresponding to the NaI solution and the (10,10) nanotube (without polarizability) measure, as before, the double difference between the ensemble-averaged values obtained with time steps of 1 and 2.5 fs and are seen to be fairly small to sustain the above interpretations.

The average ion passage times plotted in Fig. 15 as functions of the pore radius represent average time intervals during which the ions executing *successful passages* reside effectively inside the pore. This definition differs from the average time in which the channel is simply *populated* by ions, since it excludes ions barely entering the pore and reexiting to the same reservoir. Notably, the profiles shift to longer passage times with decreasing ion mass, the Na^+ ions appearing to experience the slowest translocations through the CNTs. Having in view the comparable masses of the Na^+ ion and the water molecule, it is evident that the more effective momentum transfer between them, as compared with the other ion species, contributes to more sinuous paths taken by the transiting Na^+ ions and to a more effective slowdown.

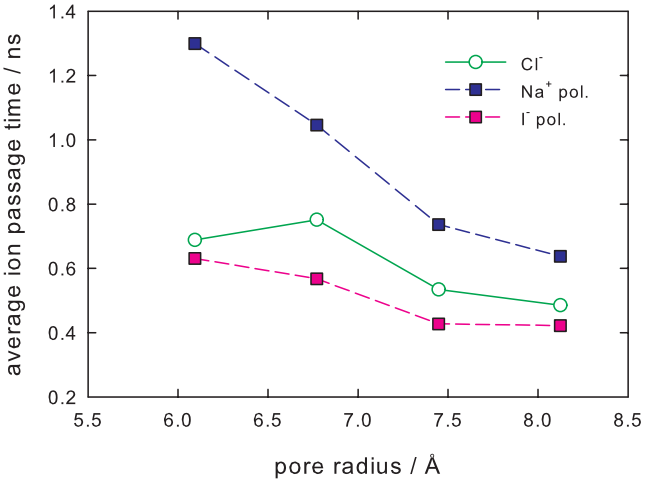

FIG. 15. Average passage times of the ions for the NaCl and NaI solutions as functions of the nanotube radius. The separate contributions of the Na^+ ions are plotted with blue lines. Filled symbols and dashed lines indicate the usage of polarizable models.

The ion passage times range, regardless of the ionic species and inclusion of polarizability, between 0.4 and 1.3 ns, showing a gradual decrease with the nanotube radius as the trajectories become less sinuous and the resistance opposed by the nanotube (measured by the average axial PMF and electrostatic potential barrier), decreases. The corresponding average velocities cover the interval of 45–150 Å/ns. The passage times derived for the spurious ion passages through the (8,8) CNT involve huge mean standard deviations, since they correspond to virtually vanishing currents and have therefore not been represented. The passage times for the (9,9) CNT appear to be still affected by appreciable errors, but are consistent with the general trend. For the (10,10) CNT there is a qualitative agreement between the average passage time for Na^+ (~1 ns) and the value reported by Peter and Hummer[19] (~1.5 ns), which is probably affected by larger fluctuations, since it corresponds to a roughly three times shorter CNT and a more than 30 times shorter data collection time.

The description of the water and ion transport through the pore in terms of diffusion coefficients requires special techniques, since the mobility is affected in the narrow CNTs by significant fluctuations due to the relatively small number of transiting ions. For the evaluation of the diffusion coefficient, we have implemented the Green–Kubo expression, which is based on the time integrated velocity autocorrelation function.[28] In order to improve the quality of the results, besides ensemble averaging, we have also chosen dynamically the velocity sampling intervals for each solution component, by resetting the time origin whenever, due to velocity decorrelation, the relative contributions to the autocorrelation functions become irrelevant.

The diffusion coefficients calculated for the water molecules, the Na^+ cations, and the Cl^- anions are listed in Table IV and can be seen to increase monotonically with the pore radius. The increase for the (12,12) CNT as compared with the (10,10) CNT amounts to more than 20% for water and Cl^-. The diffusion coefficients also grow for the wider CNTs from water to Cl^-. In the particular case of the (10,10) CNT,

TABLE IV. Diffusion coefficients of water and ions inside the pore and in the bulk solution (in $Å^2/ps$).

	H_2O	Na^+	Cl^-
(10,10)	0.205	0.261	0.260
(11,11)	0.244	0.273	0.290
(12,12)	0.248	0.281	0.320
Bulk	0.403	0.522	0.514

it is worth noting the fair agreement of the diffusion coefficients for ions (~0.26 $Å^2/ps$) with the value 0.23 ± 0.02 $Å^2/ps$ reported by Peter and Hummer.[19] For the bulk solution we find mobilities which are roughly twice the ones for the (10,10) CNT.

The reduced mobilities in the pores as compared with the bulk reflect, on one hand, the constrained flow along the cylindrical layers, and, on the other hand, by virtue of the quite close values for water and ions, the fact that the ions travel partially surrounded by their solvation shells. The latter finding is supported also by the water flux accompanying each exiting ion. Obviously, the water fluxes caused by the transiting ions cancel on average. The larger mobility of Cl^- as compared with Na^+ in the wider CNTs is perfectly consistent with the partial currents discussed above, the ratio of the diffusion coefficients matching the current ratios for Na^+ and Cl^-.

As a general finding one may note the somewhat smoother profiles suggesting more stable flows in the cases where polarizability is being accounted for, despite the fact that, as mentioned before, the ensembles of partial trajectories comprise for each particular nanotube only 0.2 μs, as compared with 0.4 μs when polarizability is being neglected.

IV. CONCLUSIONS

Systematic MD simulations of the ion transport through armchair-type CNTs of length 60.17 Å and chiralities ranging from (8,8) to (12,12) (radii from 5.42 to 8.12 Å), embedded in explicit membranes with graphene walls, filled with NaCl and NaI solutions (0.83*M*) and subject to a moderate electric field (0.02 V/Å) are reported.

The simulations show clearly that the detailed molecular structure of the solution inside the nanopore is crucial to understanding the ion permeation process. The results are consistent and extrapolate those from the literature (e.g., Peter and Hummer[19] and Corry[22]), confirming that ions face significant energy barriers and can pass only through CNTs with chiralities higher than (7,7).

The spatial density profiles evidence that the solution is highly structured in the vicinity of the carbon walls, featuring similar and almost invariant radial and axial patterns, independent of the CNT size. The structures of cylindrical (planar) water layers formed inside the channel (at the membrane) enclose alternating regions of peaking solute ion density. The water boundary layer is formed invariably independent of the solute type, with/without polarizability, both inside the pore and at the membrane walls at a distance of

roughly 3.2 Å for all nanotube radii. Equally, the densities of the I^- and Na^+ ions peak unchangingly at about 4.1 and, respectively, 5.0 Å from the carbon walls.

The only exception from the invariant order of the radial density peaks is represented by the Cl^- anions, which, inside the narrower (8,8) and (9,9) CNTs, are accommodated preferentially between the water boundary layer and the inner Na^+ layer, while in the wider pores the Cl^- ions are translocated on average closer to the axis inside the Na^+ layer.

It is worth mentioning that even though the inclusion of polarizable models for water and ions increases substantially the I^- ion density in the proximity of the water boundary layers, the overall solution structure is affected only insignificantly in terms of density peak positions. Thus, a genuine relocation of the I^- ion similar to the surface affinity phenomenon found in the case of solution/air interfaces and mediated by polarizability cannot be identified.

The axial PMF profiles confirm the preference of the anions to reside on average within the reservoirs. While inside the wider CNTs the PMF profiles are almost flat and ion nonspecific, the ion motion appearing to be almost frictionless, the narrow (8,8) CNT exhibits ion-dependent free energy barriers with nonvanishing slopes, implying less probable translocations for all ion species, and, in particular, creates a difference between the two anion species, showing a slightly lower free energy barrier for I^-.

The pore radius dependence of the transversely averaged electrostatic potential drop across the channel is almost linear and clearly insensitive to the solute type or consideration of polarizability. The average potential barriers which have to be overcome by the ions to enter the pore are significantly higher than the voltage between the channel ends caused by the applied electric field solely and decrease with increasing pore radius. They are clearly a consequence of the formation of electrical double layers at the membrane walls, which neutralize the external electric field inside the reservoirs.

Significant conclusions regarding the translocation dynamics of the ions can be drawn from the strong pore radius dependence of the ionic currents. The current profiles are roughly parabolic and practically vanish for the (8,8) nanopore, the latter finding being consistent with the results of Dzubiella *et al.*,[17,18] Peter and Hummer,[19] and Corry.[22] Taking as reference the (8,8) CNT, a modest increase of about 11% in the channel radius produces over six times more intense currents through the (9,9) CNT, while a 33% increase produces over 30 times more intense currents through the (12,12) CNT. It is quite evident that the strong dependence of the permeability on the pore radius provides a convenient gating mechanism also for biological ion channels.

Notably, a distinct selectivity of the CNTs with respect to the anion species can be identified, the total currents corresponding to the NaI solution exceeding on average by 30% the ones for the NaCl solution. This apparently surprising finding is consistent with the radial structure of the solution inside the pores, specifically with the fact that the I^- anions transit the CNTs preferentially via cylindrical layers of larger average radius. Further arguments are provided by the lower free energy barrier and the shorter passage times through the pore found for the I^- ions as compared with the Cl^- ions. In addition, the more massive I^- ions take part in less effective momentum transfer processes with water, being thus less efficiently slowed down.

The diffusion coefficients characterizing the flow through the CNTs provide a perfectly consistent description with the one based on the ion currents. In particular, in the case of the (10,10) CNT, the mobilities of water and ions are practically two times lower than in the bulk, and there is a fair agreement of the diffusion coefficient for ions (0.26 $Å^2$/ps) with the value reported by Peter and Hummer.[19]

Consideration of polarizable models for water and solute ions appears to have little relevance for the ionic currents, indicating that extensive nanofluidic simulations measuring dynamic quantities can be carried out, in principle, with appreciable accuracy and reasonable computational effort disregarding polarizability.

The ion passage times range between 0.4 and 1.3 ns and are consistent with the estimations of Peter and Hummer, showing a gradual decrease with the nanotube radius. With decreasing ion mass, the ion passage times shift to longer values, the light Na^+ ions featuring the slowest and most sinuous translocation paths through the CNTs.

ACKNOWLEDGMENTS

The author gratefully acknowledges the support by CNCSIS PN-II Grant Nos. 502 and 506.

APPENDIX A: ELECTROSTATICS

The real-space contributions to the total energy and the Coulomb force acting on a given particle i are the ones prescribed by the standard Ewald sum method,

$$E^{(r)} = \frac{1}{2}\sum_{n\in\mathbb{Z}^3}\sum_{i,j=1}^{N} q_i q_j \frac{\mathrm{erfc}(\alpha|\mathbf{r}_{ij}+\mathbf{L}_n|)}{|\mathbf{r}_{ij}+\mathbf{L}_n|},$$

$$\mathbf{F}_i^{(r)} = q_i\sum_{j=1}^{N} q_j \sum_{n\in\mathbb{Z}^3}\left[\frac{2\alpha}{\sqrt{\pi}}\exp(-\alpha^2|\mathbf{r}_{ij}+\mathbf{L}_n|^2) + \frac{\mathrm{erfc}(\alpha|\mathbf{r}_{ij}+\mathbf{L}_n|)}{|\mathbf{r}_{ij}+\mathbf{L}_n|}\right]\frac{\mathbf{r}_{ij}+\mathbf{L}_n}{|\mathbf{r}_{ij}+\mathbf{L}_n|^2}, \quad \text{(A1)}$$

where α is the space-splitting parameter and $\mathbf{L}_n$ is the translation vector of the simulation cell replicas.

The reciprocal-space contributions to the electrostatic field are treated according to the P^3M method,[30,31] which replaces the real charge distribution with an equivalent mesh-based distribution $\rho_M(\mathbf{r}_p)$ by using a charge assignment function $W(\mathbf{r}_p-\mathbf{r}_i)$,

$$\rho_M(\mathbf{r}_p) = \frac{1}{V_h}\sum_{i=1}^{N} q_i W(\mathbf{r}_p - \mathbf{r}_i),$$

$$\tilde{W}(\mathbf{k}) = V_h \left[\frac{\sin\left(\frac{1}{2}k_x h_x\right)}{\frac{1}{2}k_x h_x} \frac{\sin\left(\frac{1}{2}k_y h_y\right)}{\frac{1}{2}k_y h_y} \frac{\sin\left(\frac{1}{2}k_z h_z\right)}{\frac{1}{2}k_z h_z} \right]^P . \tag{A2}$$

Here $\mathbf{r}_p$ are the mesh points, h_x, h_y, and h_z are the mesh spacings, $V_h = h_x h_y h_z$ is the corresponding volume element, and $\tilde{W}(\mathbf{k})$ is the Fourier transformed charge assignment function.

Within the P^{3}M method, the role of the standard Coulomb Green's function $4\pi/k^2$ is taken by the optimal influence function $G_{\text{opt}}(\mathbf{k})$, which can be adjusted for the given simulation cell geometry as to make the result of the mesh calculation most closely resemble the continuum solution,

$$G_{\text{opt}}(\mathbf{k}) = \frac{i\mathbf{k}\sum_{m\in\mathbb{Z}^3}\left[\frac{1}{V_h}\tilde{W}(\mathbf{k}+\mathbf{k}_m)\right]^2 \tilde{\mathbf{R}}(\mathbf{k}+\mathbf{k}_m)}{k^2\left\{\sum_{m\in\mathbb{Z}^3}\left[\frac{1}{V_h}\tilde{W}(\mathbf{k}+\mathbf{k}_m)\right]^2\right\}^2},$$

$$\tilde{\mathbf{R}}(\mathbf{k}) = -i\mathbf{k}\frac{4\pi}{k^2}\exp\left(-\frac{k^2}{4\alpha}\right), \tag{A3}$$

where $\mathbf{k}_m = (2\pi m_x/h_x, 2\pi m_y/h_y, 2\pi m_x/h_x)$. One of the advantageous features of the P^{3}M approach is also the provision of prescriptions for determining the optimal space-splitting Ewald parameter α.

The k-space electrostatic field that resulted by solving the Poisson equation for the Fourier-transformed mesh-based charge distribution $\tilde{\rho}_M(\mathbf{k}) = \overrightarrow{\text{FFT}}[\rho_M(\mathbf{r}_p)]$ is transformed back to real space as a mesh-based field,

$$\Phi^{(k)}(\mathbf{r}_p) = \overleftarrow{\text{FFT}}[\tilde{\rho}_M(\mathbf{k}) \times G_{\text{opt}}(\mathbf{k})](\mathbf{r}_p),$$

$$\mathbf{E}^{(k)}(\mathbf{r}_p) = \overleftarrow{\text{FFT}}[-i\mathbf{k} \times \tilde{\rho}_M(\mathbf{k}) \times G_{\text{opt}}(\mathbf{k})](\mathbf{r}_p), \tag{A4}$$

where $i\mathbf{k}$ differentiation in reciprocal space is used to obtain the electric field $\mathbf{E}^{(k)}(\mathbf{r}_p)$. The mesh-based field is then reprojected onto the real particles by using the charge assignment function to yield the reciprocal space contributions to the total energy and to the electrostatic forces acting on them,

$$E^{(k)} = \sum_{i=1}^{N} q_i \sum_{\mathbf{r}_p \in M}^{N} \Phi^{(k)}(\mathbf{r}_p) W(\mathbf{r}_i - \mathbf{r}_p),$$

$$\mathbf{F}_i^{(k)} = q_i \sum_{\mathbf{r}_p \in M}^{N} \mathbf{E}^{(k)}(\mathbf{r}_p) W(\mathbf{r}_i - \mathbf{r}_p). \tag{A5}$$

The ensemble-averaged electrostatic potential due to the particles and external fields is obtained by solving the Poisson equation for the ensemble-averaged mesh-based charge distribution in reciprocal space by using the same three-dimensional grid as for the P^{3}M Ewald method,

$$\Phi(\mathbf{r}_p) = \overleftarrow{\text{FFT}}\left[\frac{4\pi}{k^2}\overrightarrow{\text{FFT}}[\langle\rho_M(\mathbf{r}_p)\rangle](\mathbf{k})\right](\mathbf{r}_p). \tag{A6}$$

In particular, for the five nanotubes considered in the present study we considered a regular $32\times32\times128$ point grid and a seventh-order charge assignment function ($P=7$). The optimal Ewald space-splitting parameters ranged depending on the pore radius between 0.360 99 and 0.363 84.

APPENDIX B: BENCHMARK SIMULATIONS

With a view to assess the general strategy and the various models adopted in the present study, with special emphasis on the COS models used for polarizability, preliminary benchmark simulations have been performed similar to the ones of Jungwirth and Tobias[39] using the AMBER package.[40] The simulations of Jungwirth and Tobias[39] have shown for sodium halide solution/air interfaces a qualitatively different surface affinity, in marked dependence on the ion size and polarizability. Specifically, the larger, more polarizable halide anions (iodide and bromide) are present at the interface, and actually have higher concentrations in the interfacial region than in the bulk, unlike the smaller and less polarizable ones (fluoride and chloride).

Aiming for improved statistics and smoother density profiles, we have simulated a larger system (composed of 1000 water molecules, 22 Na^+ cations, and 22 halide anions), considering for each case a larger data collection time (20 ns) based on four different trajectories, each on its part started from a different random initial configuration.

Technically, each initial configuration is prepared at first as a cube of water molecules, regularly disposed but randomly oriented on a rectangular grid corresponding to a density of 1 g/cm^3, with the ions placed randomly in the interstices. The cubic simulation cell is then augmented symmetrically along the z-axis on both sides with empty space up to the threefold of the initial extent, with the final dimensions $31.04\times31.04\times93.13$ Å^3. The preparation of the initial configuration is completed by equilibrating the system for 1 ns.

The density profiles that resulted for the NaCl and NaI solutions (with and without polarizability and using the TIP4P and COSG2 water models, respectively) are presented in Fig. 16. It can be easily seen that in the case of the NaCl solution (upper panel), both ion species are accommodated rather uniformly in the bulk, while the interface is depleted, irrespective of the inclusion of polarizability. Quite in contrast, in the case of NaI (lower panel), the behavior of the iodine anions at the interface is strongly affected by the polarizability, resulting in a marked surface affinity when polarizability is being accounted for. In the latter case, the Na^+ ions peak themselves, too, however, beneath the interface. This behavior matches perfectly the one emerging from the simulations of Jungwirth and Tobias.

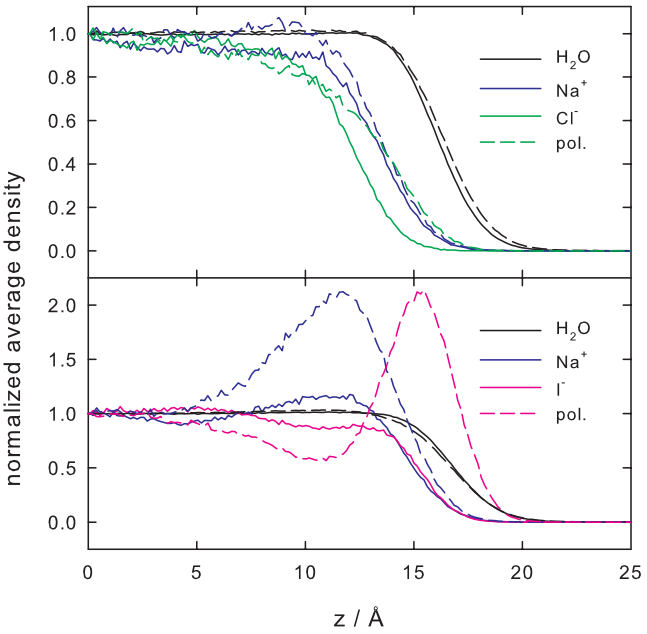

FIG. 16. Average transverse density profiles of water and ions for the NaCl and NaI solution/air interfaces. Dashed lines indicate the usage of polarizable water and ion models. All profiles are normalized to their bulk value.

APPENDIX C: INITIAL CONFIGURATIONS

Pursuing the idea of improving statistics and reducing time correlations for all ensemble-averaged quantities, in addition to considering sufficiently long total simulation times and a sufficiently large number of independent trajectories, special attention was devoted to the preparation of the distinct starting configurations. Specifically, each particular initial configuration is prepared at first as a cubic arrangement of water molecules, disposed regularly but oriented randomly on a rectangular grid, with the ions placed randomly in the interstices. The cubic simulation cell is then split symmetrically by a plane perpendicular to the z-axis, giving rise to the two reservoirs, and the nanotube is inserted in between.

The concrete value of the effective total volume which should be accessible results directly from the number of handled water molecules and the desired density ($1\ \mathrm{g/cm^3}$). It is essential, however, to note that the initial cubic volume in which the solution is concentrated is not the entire effective volume, but just the difference between this one and the effective pore volume, and corresponds evidently to a water density higher than $1\ \mathrm{g/cm^3}$. In this manner, after splitting the cube and the setup of the actual nanotube and its two reservoirs, the volume accessible to the solution matches in fact the correct effective total volume. Any final fine tuning of the simulation cell can then be accomplished by adjusting its z_{cell} dimension.

From the particular arrangement, with densely filled reservoirs and completely empty channel, one needs simply to conduct a smooth NVT equilibration to obtain the "final" initial configuration by allowing the solution to relax freely into the channel. A duration of 1 ns with a time step of 1 fs proved to be sufficient for equilibrium to set in for all nanotube geometries.

The main advantage of the presented initialization protocol is that it allows for an accurate control of the solution density, circumventing completely the need of additional PVT equilibration runs and, thus, avoiding the possible distortion of the whole simulation cell and of the CNT itself. In addition, the initial flow of the solution into the pore introduces a high degree of microscopic hazard in a natural way.

[1] S. Iijima, Nature (London) **354**, 56 (1991).
[2] *Carbon Nanotubes: Advanced Topics in the Synthesis, Structure, Properties and Applications*, edited by A. Jorio, G. Dresselhaus, and M. S. Dresselhaus (Springer, New York, 2008).
[3] J. Liu, A. G. Rinzler, H. Dai, J. H. Hafner, R. K. Bradley, P. J. Boul, A. Lu, T. Iverson, K. Shelimov, C. B. Huffman, F. Rodriguez-Macias, Y.-S. Shon, T. R. Lee, D. T. Colbert, and R. E. Smalley, Science **280**, 1253 (1998).
[4] D. A. Walters, M. J. Casavant, X. C. Qin, C. B. Huffman, P. J. Boul, L. M. Ericson, E. H. Haroz, M. J. O'Connell, K. Smith, D. T. Colbert, and R. E. Smalley, Chem. Phys. Lett. **338**, 14 (2001).
[5] K. Hata, D. N. Futaba, K. Mizuno, T. Namai, M. Yumura, and S. Iijima, Science **306**, 1362 (2004).
[6] S. Talapatra, S. Kar, S. K. Pal, R. Vajtai, L. Ci, P. Victor, M. M. Shaijumon, S. Kaur, O. Nalamasu, and P. M. Ajayan, Nat. Nanotechnol. **1**, 112 (2006).
[7] T. Yamada, T. Namai, K. Hata, D. N. Futaba, K. Mizuno, J. Fan, M. Yudasaka, M. Yumura, and S. Iijima, Nat. Nanotechnol. **1**, 131 (2006).
[8] B. J. Hinds, N. Chopra, T. Rantell, R. Andrews, V. Gavalas, and L. G. Bachas, Science **303**, 62 (2004).
[9] J. K. Holt, A. Noy, T. Huser, D. Eaglesham, and O. Bakajin, Nano Lett. **4**, 2245 (2004).
[10] J. Holt, H. Park, Y. Wang, M. Stadermann, A. Artyukhin, C. Grigoropolous, A. Noy, and O. Bakajin, Science **312**, 1034 (2006).
[11] M. Monthioux, Carbon **40**, 1809 (2002).
[12] G. Hummer, J. C. Rasaiah, and J. P. Noworyta, Nature (London) **414**, 188 (2001).
[13] V. P. Sokhan, D. Nicholson, and N. Quirke, J. Chem. Phys. **117**, 8531 (2002).
[14] D. Nicholson and N. Quirke, Mol. Simul. **29**, 287 (2003).
[15] S. Supple and N. Quirke, Phys. Rev. Lett. **90**, 214501 (2003).
[16] S. Supple and N. Quirke, J. Chem. Phys. **121**, 8571 (2004); **122**, 104706 (2005).
[17] J. Dzubiella, R. J. Allen, and J.-P. Hansen, J. Chem. Phys. **120**, 5001 (2004).
[18] J. Dzubiella and J.-P. Hansen, J. Chem. Phys. **122**, 234706 (2005).
[19] C. Peter and G. Hummer, Biophys. J. **89**, 2222 (2005).
[20] I. Hanasaki and A. Nakatani, J. Chem. Phys. **124**, 174714 (2006).
[21] H. Liu, S. Murad, and C. J. Jameson, J. Chem. Phys. **125**, 084713 (2006).
[22] B. Corry, J. Phys. Chem. B **112**, 1427 (2008).
[23] M. Whitby, L. Cagnon, M. Thanou, and N. Quirke, Nano Lett. **8**, 2632 (2008).
[24] T. A. Hilder, D. Gordon, and S.-H. Chung, Small **5**, 2183 (2009).
[25] P. S. Crozier, R. L. Rowley, N. B. Holladay, D. Henderson, and D. D. Busath, Phys. Rev. Lett. **86**, 2467 (2001).
[26] P. S. Crozier, D. Henderson, R. L. Rowley, and D. D. Busath, Biophys. J. **81**, 3077 (2001).
[27] T. A. Beu, J. Optoelectron. Adv. Mater. **8**, 160 (2006).
[28] D. C. Rapaport, *The Art of Molecular Dynamics Simulation* (Cambridge University Press, Cambridge, England, 1995).
[29] H. Goldstein, *Classical Mechanics*, 2nd ed. (Addison-Wesley, Reading, MA, 1980).
[30] R. W. Hockney and J. W. Eastwood, *Computer Simulation Using Particles* (IOP, Bristol, 1988).
[31] M. Deserno and C. Holm, J. Chem. Phys. **109**, 7678 (1998); **109**, 7694 (1998).
[32] W. L. Jorgensen, J. Chandrasekhar, J. D. Madura, R. W. Impey, and M. L. Klein, J. Chem. Phys. **79**, 926 (1983).
[33] M. W. Mahoney and W. L. Jorgensen, J. Chem. Phys. **112**, 8910 (2000).
[34] H. Yu and W. F. van Gunsteren, J. Chem. Phys. **121**, 9549 (2004).
[35] T. P. Straatsma and J. A. McCammon, Mol. Simul. **5**, 181 (1990).
[36] D. E. Smith and L. X. Dang, J. Chem. Phys. **100**, 3757 (1994).
[37] L. X. Dang, J. Phys. Chem. B **106**, 10388 (2002).

[38] G. Markovich, L. Perera, M. L. Berkowitz, and O. Cheshnovsky, J. Chem. Phys. **105**, 2675 (1996).
[39] P. Jungwirth and D. J. Tobias, J. Phys. Chem. B **105**, 10468 (2001).
[40] D. A. Case, T. A. Darden, T. E. Cheatham III, C. L. Simmerling, J. Wang, R. E. Duke, R. Luo, M. Crowley, R. C. Walker, W. Zhang, K. M. Merz, B. Wang, S. Hayik, A. Roitberg, G. Seabra, I. Kolossváry, K. F. Wong, F. Paesani, J. Vanicek, X. Wu, S. R. Brozell, T. Steinbrecher, H. Gohlke, L. Yang, C. Tan, J. Mongan, V. Hornak, G. Cui, D. H. Mathews, M. G. Seetin, C. Sagui, V. Babin, and P. A. Kollman, *AMBER 10* (University of California, Berkeley, 2008).